3. Chapter 3: Integration of $Pb_{1.1}(Zr_{0.53}Ti_{0.47})O_3$ (PZT) capacitors into high density memory structure using iridium based bottom electrodes.

3.1 Abstract

We have investigated the feasibility of IrO_2/Ir multi-layered structure as a simple electrode-barrier for $Pb(Zr,Ti)O_3$ (PZT) based nonvolatile memories. A multilayer of IrO_2/Ir was rf-sputtered onto a poly-Si coated Si wafer. PZT thin films deposited onto these as-deposited IrO_2/Ir electrodes possessed large amounts of pyrochlore phase and intermediate reaction layer of Pb-Ir-O. In addition to the perovskite phase, these PZT films exhibited a secondary phase arising out of stoichiometric imbalance in the films. Accordingly, PZT capacitors based on as-deposited IrO_2/Ir electrodes showed poor fatigue and leakage current behaviors. By annealing the bottom IrO_2/Ir electrodes in a vacuum of $1x10^{-5}$ torr in the temperature range of 100 ^oC to 400 ^oC, we could carefully control the microstructural development of PZT thin films. PZT thin film deposited on annealed IrO_2/Ir (annealed at 280 ^oC) was found to be comprised of pure perovskite phase with no reaction layer or secondary phase. Based on this study, we have successfully prepared Ir/IrO_2/PZT/annealed IrO_2/Ir/poly-Si capacitors, whose polarization loss was 12 % after 10^{11} switching cycles and a leakage current density of $1x10^{-7}$ A/cm^2 at an applied field of 200 kV/cm.

3.2 Introduction

Recently, extensive researches have been performed to accomplish high-density integration of PZT based nonvolatile ferroelectric random access memories (NvFRAMs). High density NvFRAMs require one transistor-one capacitor (1T-1C) memory cell structure[1] with the bottom electrode of the capacitor in direct contact with a poly-Si plug, which in turn is connected to the source or the drain of the transistor in the memory cell. Such a stacked structure is required to reduce the cell area in high-density memories. In 1T-1C cell structure, the role of bottom electrode is important, especially in PZT based capacitor, since bottom electrode is required to perform a variety of functions which include: (a) Inhibit the diffusion of oxygen towards poly-Si plug (b) Assist in developing a microstructure dominated by perovskite phase of PZT by providing appropriate nucleation sites (c) Enhance the fatigue resistance of the PZT capacitor. Several electrode-barrier structures have been proposed for the integration of ferroelectric memory devices. Amongst them, Pt/TiN/$TiSi_2$[2] is a typical low temperature electrode-barrier for PZT based capacitors. PZT thin film capacitors processed at temperatures of 650 ^oC on Pt electrodes have a well developed perovskite phase with minimal pyrochlore phase and a large remnant polarization, but their remanent polarization and leakage current density are easily degraded by repeated polarization reversals (fatigue).

Extensive researches have been devoted to understanding the mechanisms responsible for such degradations, and to improving/removing the degradation by using conductive oxide electrodes, such as LSCO[3], RuO_2[4] and IrO_2[5], and hybrid electrodes, such as Pt/RuO_2[6], Pt/IrO_2[7] and Ir/IrO_2[7]. The idea behind the use of conductive oxide electrode was to provide enough oxygen concentration at the PZT/electrode interface that would

help in increasing the fatigue resistance of PZT capacitor. However, use of such conductive oxides reduced the crystallinity of the PZT thin film resulting in the formation of undesirable secondary phases, which reduced the remnant polarization and the leakage resistivity of PZT capacitor. Also, these oxide electrodes were not stable at high processing temperatures (> 600 ^{o}C). High temperature electrode-barrier structures like $PtRhO_x/PtRh/PtRhO_x$[8] and $Pt/IrO_2/Ir$[9] resulted in remarkable ferroelectric behaviors, such as low polarization fatigue and low leakage current density for PZT based capacitors. However, large thickness of these electrode-barrier structures (above 200 nm) as well as more complex integration procedures (hybrid type electrodes) may be unsuitable for the integration of NvFRAMs. Hence, development of a simple and thin electrode-barrier structure is necessary from the practical aspect point of view.

Electrode materials applicable to the simple electrode-barrier structure are typically noble metals, such as Pt, Ru and Ir. Pt cannot prevent the diffusion of oxygen. Further, Ru as well as Pt easily react with Si to form a silicide even at temperatures as low as 400 ^{o}C. On the other hand, Ir can prevent the diffusion of oxygen[10] and has no contact problems with silicon for processing temperatures lower than 600 ^{o}C. Hence, in the present work, we have employed IrO_2/Ir structure as the bottom-electrode for the PZT based capacitors. While Ir layer inhibits the diffusion of oxygen towards the poly-Si plug, the Ir oxide layer assists in increasing the fatigue resistance of PZT capacitor. Fatigue and leakage current resistance were further improved by subsiding the growth of secondary phases in PZT films. In order to eliminate the formation of undesirable secondary phases, we have controlled the microstructural development of PZT thin film by modifying the surface of IrO_2/Ir electrode. The bottom IrO_2/Ir electrode was annealed in vacuum so that

appropriate nucleation sites for the growth of perovskite rich films could be obtained. The current paper is divided into two parts. In the first part, we show the necessity for modification of the surface composition and surface structure of as-deposited IrO_2/Ir electrode on the basis of fatigue and leakage current behaviors of PZT capacitors. In the second part, we show the optimization of processing conditions for annealing of IrO_2/Ir electrodes deposited on poly-Si substrates in order to obtain both minimal fatigue and low leakage current in PZT capacitors.

3.3 Experimental

Ir-layer of 80 nm thickness and thin IrO_2-layer of 20 nm thickness were deposited onto n^+ poly-Si/SiO_2/Si wafers using an *in-situ* rf-sputtering process in pure Ar and Ar+O_2 ambiance, respectively. The partial pressure of Ar and O_2 were $2.0x10^{-3}$ torr and $3.0x10^{-3}$ torr, respectively. The deposition rate of Ir and IrO_2 were 10 nm/min and 5 nm/min, respectively. In order to modify the surface-oxygen concentration of IrO_2 layer, after depositing the thin layer of IrO_2 onto Ir/poly-Si, the substrates were annealed at various temperatures ranging from 100 ^oC to 400 ^oC for 15 min in a vacuum of $1x10^{-5}$ torr (the so called "vacuum annealing"). The sol-gel derived PZT films of 250 nm thickness, with a composition of $Pb_{1.1}(Zr_{0.53}Ti_{0.47})O_3$, were deposited on to these substrates by using a conventional spin-coating method, which was described elsewhere[11]. A post-deposition annealing at temperatures ranging from 600 ^oC to 700 ^oC was given for 1 hr in O_2-ambiance in order to crystallize PZT thin films in ferroelectric phase. Ir/IrO_2-multilayered-top electrodes of 0.2 mm diameter were sputter-deposited on the top surface of PZT thin films using a shadow mask, where Ir was used only for strengthening the top-IrO_2 layer. The deposition conditions of top electrodes were the same as those of bottom electrode-barriers. The thickness of Ir and IrO_2 top electrodes were 80 nm and 20 nm, respectively.

All the electrical measurements on the capacitors were made between the top electrode and the surface of poly-Si. The ferroelectric properties, such as P-E hysteresis loop and polarization fatigue were measured using a standard RT66A ferroelectric tester (Radiant Technologies) and also, the fatigue tests were performed using an externally

generated square wave with an amplitude of ± 5 V and a frequency of 1 MHz. The dc electrical current-voltage characteristics of these capacitors were measured using an electrometer/source (Keithley 617). Data acquisitions of all the electrical measurements were performed using a personal computer. Vacuum annealing of the as-deposited IrO_2/Ir substrates resulted in oxygen evaporation from the IrO_2 layer. The surface compositional ratio of annealed IrO_2 thin films was determined using electron spectroscopy for compositional analysis (ESCA). X-ray diffraction (XRD) was used to determine the crystallinity of annealed IrO_2 thin films and PZT films. Auger electron spectroscopy (AES) was used to investigate the depth profiles of the elements in PZT/annealed IrO_2/Ir/poly-Si films. The surface morphologies of PZT films were investigated using an atomic force microscope (AFM).

3.4 Results and Discussion

3.4.1. PZT capacitors with as-deposited IrO_2/Ir electrode-barriers

The surface compositional ratio of Ir/O in as-deposited IrO_2 was found to be 29/71, which corresponds to $IrO_{2.4}$ (hereafter we refer 'as-deposited IrO_2' to 'IrO_2'). Figure 3.1 shows the XRD patterns of PZT/IrO_2/Ir/poly-Si annealed at temperatures of 600 ^oC, 650 ^oC and 700 ^oC (T_{post}). PZT thin films deposited on IrO_2/Ir/poly-Si were found to crystallize predominantly in (011) direction rather than in (111) direction as was observed in the case of PZT films deposited on Pt/Ti/SiO_2/Si substrates[11]. In addition, the integrated intensities of all the peaks corresponding to the perovskite phase of PZT films were found to increase, while the pyrochlore phase was found to decrease with the increase in T_{post}. Along with the crystalline phases of PZT and Ir films, two amorphous halos spread around 2θ of 28.5^o and 34.5^o (indicated by means of dotted lines in Fig. 3.1) were observed for all the three films and the integrated intensity of these amorphous halos increased as the annealing temperature was increased. A feasible explanation could be obtained from the work done by Shimizu *et al*[12], who observed an amorphous reaction layer of Pb-Ir-O between PZT layer and Ir substrate. We interpret that these halos correspond to amorphous phases of Pb-Ir-O, which might arise from the reaction of PbO in PZT with IrO_2. In the case of PZT film deposited on RuO_2, a conductive pyrochlore-type lead ruthenate ($Pb_2Ru_2O_{7-x}$) phase[13,14] was well known to be a stable crystalline phase. But, in the case of PZT films deposited on IrO_2, lead iridate (Pb-Ir-O) is an amorphous phase which is believed to be unstable. In addition, evaporation of PbO at these high annealing temperatures of 650 ^oC and 700 ^oC could have

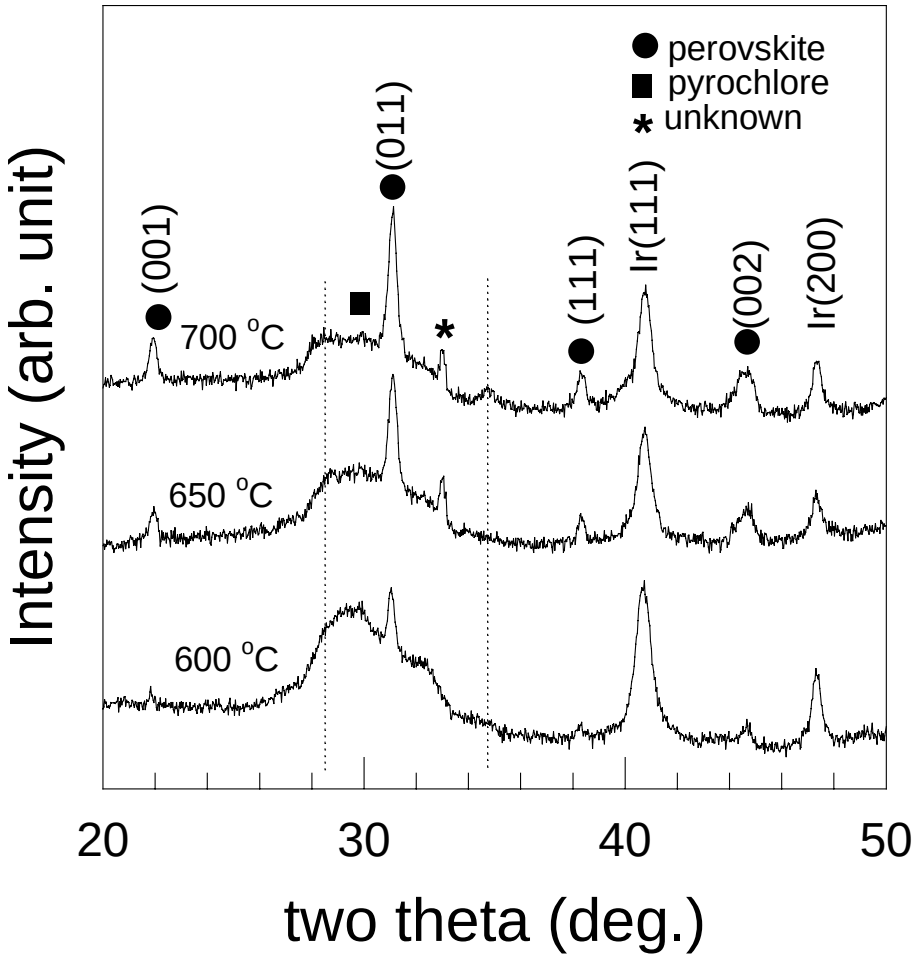

Fig. 3.1. XRD patterns of PZT/as-deposited IrO_2/Ir/poly-Si post-annealed at 600 °C, 650 °C and 700 °C.

resulted in non-stoichiometry of the PZT thin films and is manifested as extraneous peak at $2\theta = 32.8^{o}$. This secondary phase could be clearly seen in the AFM images of the corresponding PZT films.

Figure 3.2 shows the typical AFM images of the surface morphology for PZT films deposited on IrO_2/Ir processed at different T_{post}. In Fig. 3.2, the AFM image for PZT film deposited on Pt/Ti/SiO_2/Si substrate and processed at 600 ^{o}C is also shown for the purpose of comparison. The surface morphology of the PZT film deposited on IrO_2/Ir and processed at 600 ^{o}C (Fig. 3.2(a)) showed a first phase with small nanograins and a second phase with a diameter greater than 5□□m, non-uniformly distributed throughout the PZT film, while that of PZT/Pt/Ti/SiO_2/Si (Fig. 3.2(c)) showed only the first phase with small nanograins. Although the formation mechanism and structure of the second phase is not yet understood clearly, the second phase observed in the AFM images could be directly correlated or closely related to the pyrochlore phase observed in the XRD pattern of the PZT film processed at 600 ^{o}C (Fig. 3.1). Annealing of the films at higher temperatures resulted in the growth of the first phase which was clearly manifested in the fig. 3.2(b), where large grains of the first phase with a diameter greater than 1 μm were observed. These results together with the XRD results (Fig. 3.1), where the intensities of all the perovskite peaks increased with the increase in T_{post}, suggests that the first phase corresponds to the perovskite phase of the PZT film. In addition, a secondary phase was also observed in the case of PZT film annealed at 700 ^{o}C (Fig. 3.2 (b)), which might correspond to the extraneous peak observed in the XRD pattern of this particular PZT film (Fig. 3.1).

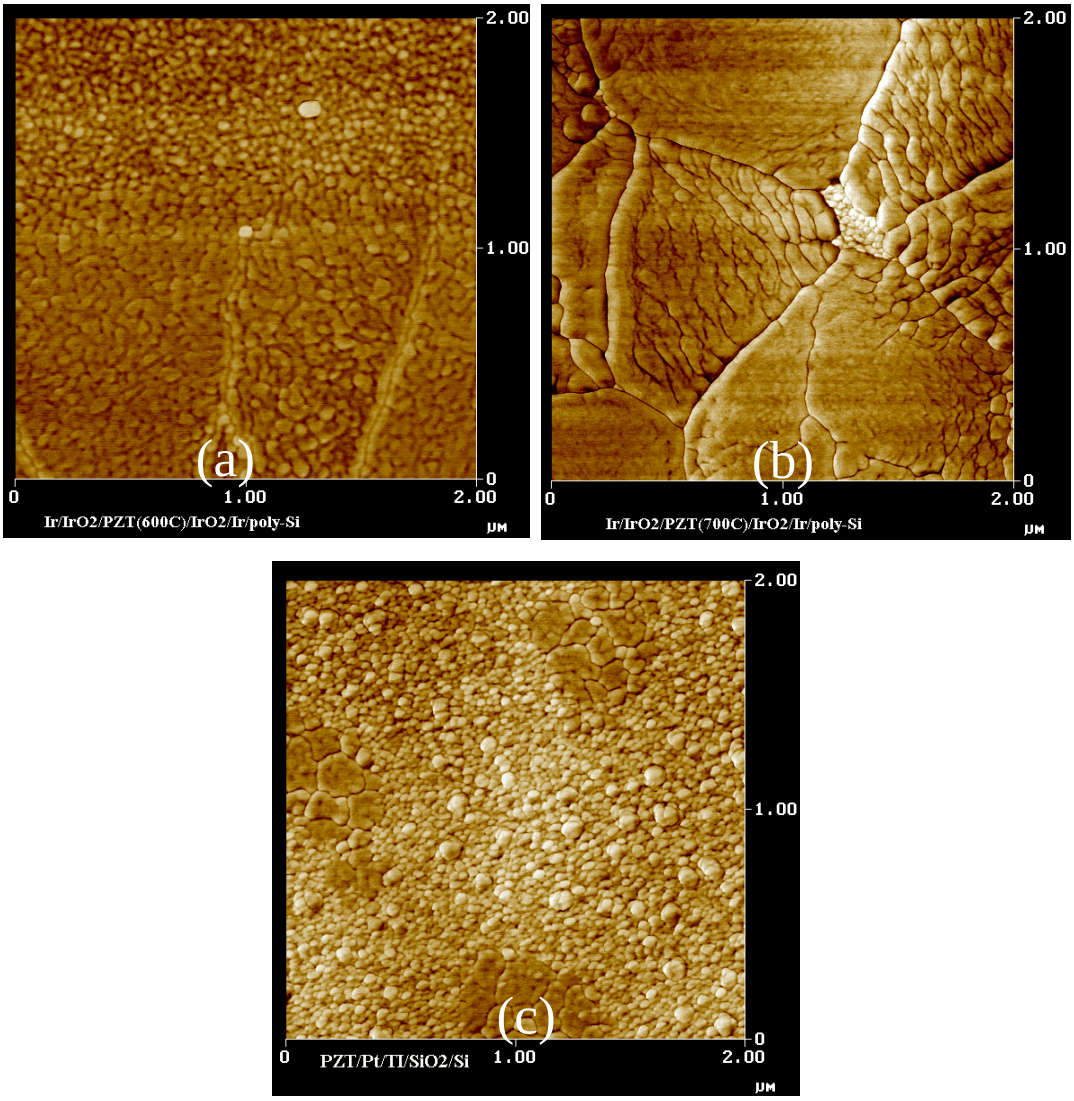

Fig. 3.2. AFM images of the surface morphologies of PZT/as-deposited IrO_2/Ir/poly-Si post-annealed at T_{post} of (a) 600 ^{o}C, (b) 650 ^{o}C and (c) PZT/Pt/Ti (600^{0}C).

PZT thin films deposited on IrO_2/Ir electrodes and processed at a lower temperature of 600 ^oC resulted in large proportion of pyrochlore phase, while the PZT films annealed at higher temperatures resulted in lower proportion of pyrochlore phase, but possessed secondary phases. Such type of microstructure had a profound effect on the electrical properties of these PZT based capacitors.

We investigated the typical electrical properties, such as P-E hysteresis loop, polarization fatigue and leakage current-voltage characteristics, of PZT thin films deposited on as-deposited IrO_2(20nm)/Ir(80nm)/poly-Si. Figure 3.3 shows P-E hysteresis loops of PZT capacitors bearing the structures of Ir/IrO_2/PZT/IrO_2/Ir, where the PZT layers were post-annealed at temperatures ranging from 600 ^oC to 700 ^oC. In Fig. 3.3, hysteresis loop of Pt/PZT/Pt capacitor is also shown for the purpose of comparison. Well-defined P-E hysteresis loops were obtained for all capacitors. The same P-E loops were also obtained even if one electrical contact was replaced from the surface of poly-Si to the bottom-Ir electrode, which indicated that IrO_2/Ir bottom electrode itself behaved as a good electrode-barrier even at a high processing temperature of 700 ^oC. Ir/IrO_2/PZT/IrO_2/Ir capacitor with T_{post}=700 ^oC exhibited a P_r close to that of Pt/PZT/Pt capacitor. Remanent polarization (P_r) increased remarkably with the increase in T_{post} of PZT layer. Such a trend could be attributed to the increase in the grain size of the perovskite phase with the increase in the annealing temperature. On the other hand, the behaviors of polarization fatigue and leakage current of Ir/IrO_2/PZT/IrO_2/Ir could be explained based on the distribution of intermediate reaction layer and the secondary phase. Figure 3.4 shows the polarization-fatigue behaviors of these PZT capacitors. In

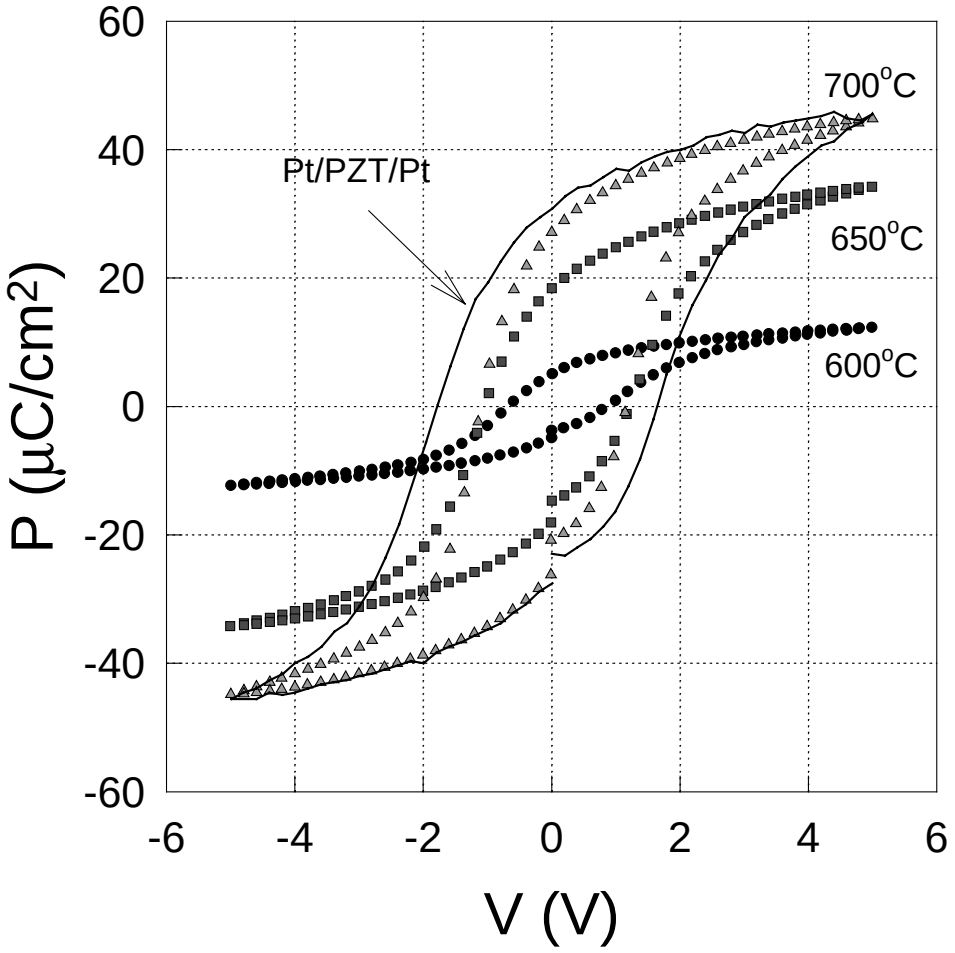

Fig. 3.3. P-E hysteresis loops of Ir/IrO_2/PZT/IrO_2/Ir/poly-Si, where IrO_2 layer has 20-nm-thickness and is as-deposited without any annealing treatment and PZT layers are post-annealed at 600 °C, 650 °C and 700 °C.

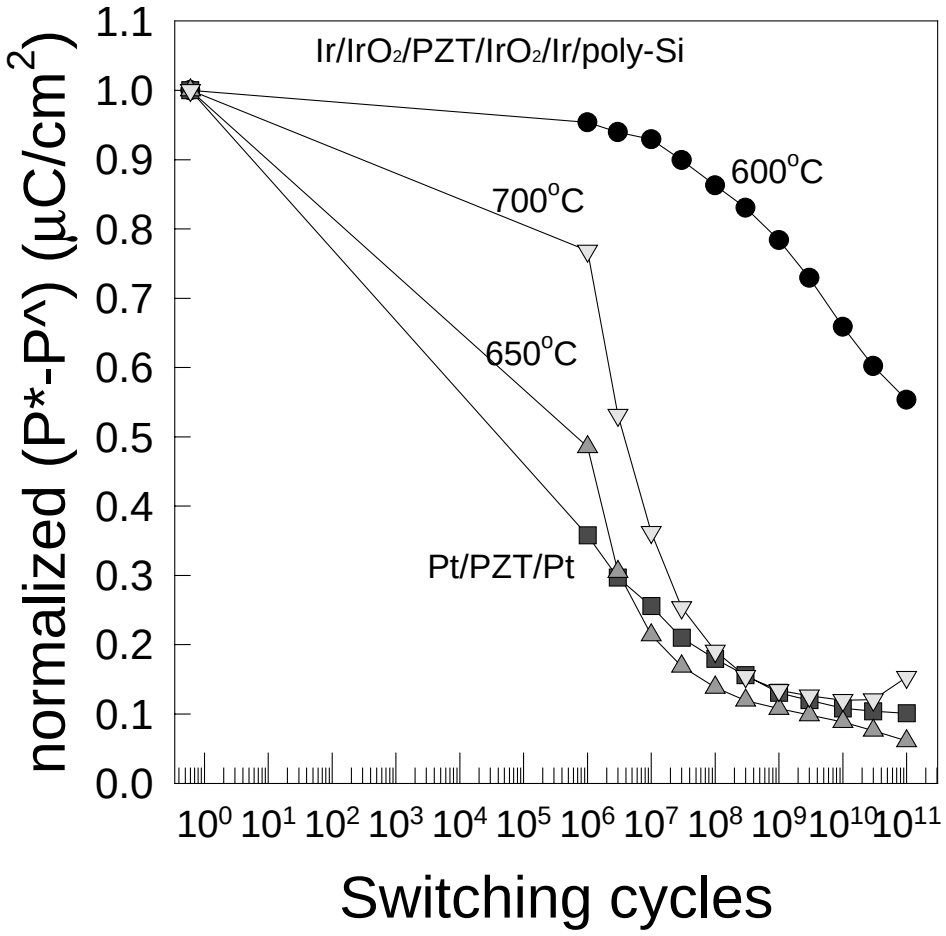

Fig. 3.4. Polarization fatigue behaviors of Ir/IrO_2/PZT/as-deposied IrO_2/Ir/poly-Si.

Fig. 3.4, the mean value of the normalized difference between the switched and non-switched polarization (P*-P^) for each polarity was plotted as a function of switching cycles applied to the capacitors. Ir/IrO_2/PZT/IrO_2/Ir capacitors with T_{post}=600 ^oC exhibited 45% polarization loss after 10^{11} cycles, which is too large to be practically used in the integration of NvFRAMs. Such a high fatigue rate could be due to the improper microstructure developed in the PZT thin films. In other words, the polarization fatigue in PZT/IrO_2/Ir structures could be attributed to the formation of Pb-Ir-O intermediate layer between PZT and bottom IrO_2, to the pyrochlore phase and also to the secondary phase in PZT, as mentioned above. Moreover, as T_{post} was increased, the polarization loss after 10^{11} cycles increased up to 90 %, which was nearly the same as that of Pt/PZT/Pt, as shown in Fig. 3.4. Accordingly, increase in fatigue in the PZT film processed at 650 ^oC and 700 ^oC could be attributed to the increased Pb-Ir-O intermediate layer and the secondary phase, as observed in the XRD pattern of these particular films (Fig. 2.1).

Figure 3.5 shows the leakage current-voltage (I-V) characteristics of Ir/IrO_2/PZT/IrO_2/Ir capacitors with different T_{post}. PZT capacitors showed higher leakage current density as T_{post} was increased. There are several types of leakage current mechanisms[15,16] in ferroelectric thin film capacitors, although the unified conduction mechanism has not been yet understood. While ohmic conduction is observed at low fields, conduction in high fields is dominated by Schottky emission[15,16] and/or Poole-Frenkel emission[16]. In Fig. 3.5, it could be seen that the regions of rapidly increased current in I-V curves appeared to shift toward lower fields region as T_{post} increased and no ohmic region was shown apparently seen in I-V curve for PZT capacitor with

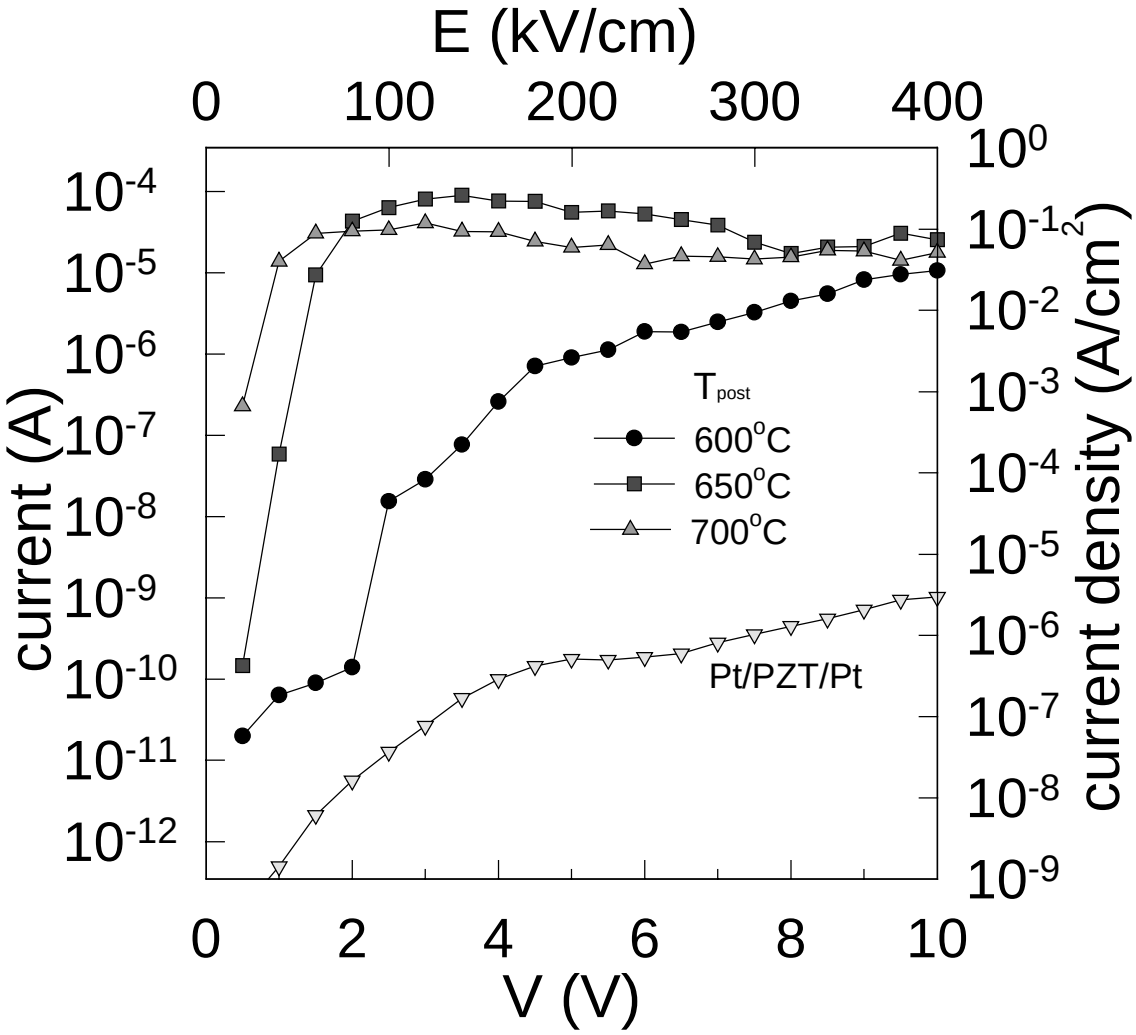

Fig. 3.5. Leakage current-voltage characteristics of Ir/IrO_2/PZT/as-deposited IrO_2/Ir/poly-Si capacitors with different T_{post}.

T_{post}=700 ^{o}C. Moreover, even at high fields region, leakage current density (J) of PZT capacitors with T_{post} larger than 650 ^{o}C was found to be constant with the applied field (E) ($J \propto E^{0}$), which

indicated that I-V behaviors of these capacitors were closely related to the distribution of the second phase, rather than to the intrinsic conduction dominated by Schottky emission That is, as T_{post} is increased, the second phase might be more well defined, as seen in the XRD patterns of these films (Fig. 3.1), and hence, leakage current of PZT capacitor with IrO_2/Ir bottom electrode could be more dominated by the second phase between PZT and IrO_2/Ir bottom electrode, which might be more conductive than the first phase of PZT.

From the above discussion, it is clear that both the fatigue and leakage current mechanisms are related to the improper development of the microstructure in PZT thin films. As the crystallization of PZT thin films is initiated by heterogeneous nucleation, an approach to develop perovskite phase dominated microstructure in PZT thin films would be to modify the IrO_2/Ir substrate surface to provide appropriate nucleation sites for perovskite phase of PZT. In order modify the surface of IrO_2/Ir electrodes, we have annealed these electrodes in a vacuum of 10^{-5}Torr at various temperatures. PZT thin films were deposited on to these modified IrO_2/Ir electrodes and were annealed at 600 ^{o}C.

3.4.2. PZT capacitors with annealed IrO_2/Ir electrode-barrier structures

Figure 3.6 shows the schematics of the preparation of PZT capacitors with annealed IrO_2/Ir electrode-barrier, where annealing process of IrO_2 layer was performed at different temperatures (T_{ann}) in a vacuum of $1x10^{-5}$ torr (Fig. 3. 6(b)) and post-

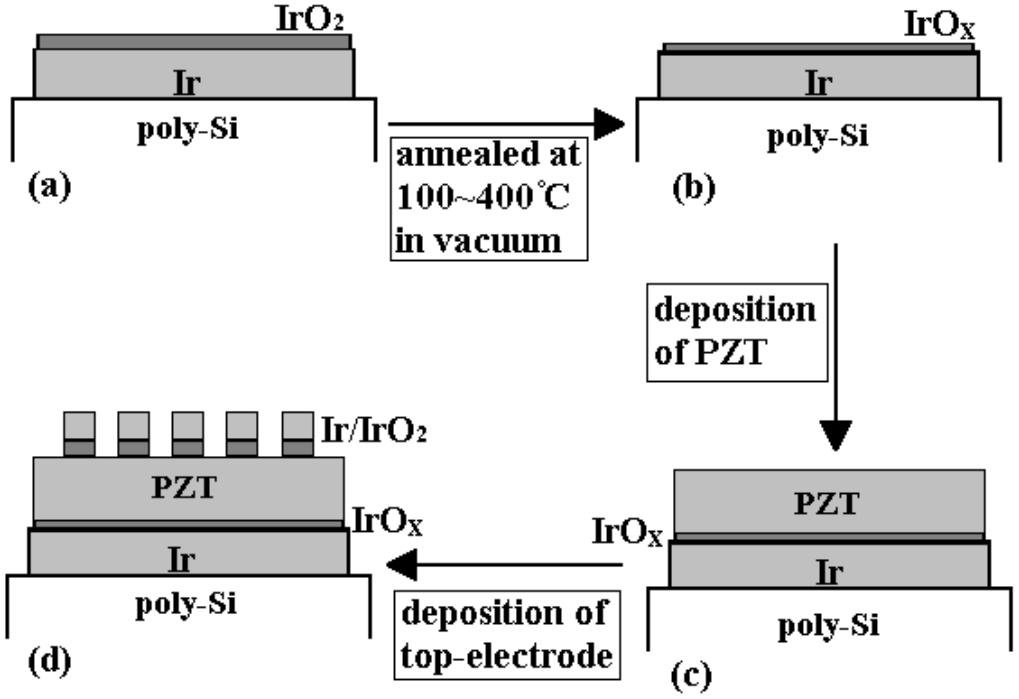

Fig. 3.6. Schematic of the preparation of PZT(53/47) thin film on to annealed IrO_2/Ir/poly-Si substrate, in which each step is as denoted below: (a) In-situ deposition of IrO_2/Ir onto poly-Si, (b) Annealing process of IrO_2 in a vacuum of $1x10^{-5}$ torr, (c) Deposition of sol-gel derived PZT layer which is annealed at 600 ^oC, (d) Deposition of top electrode (Ir/IrO_2).

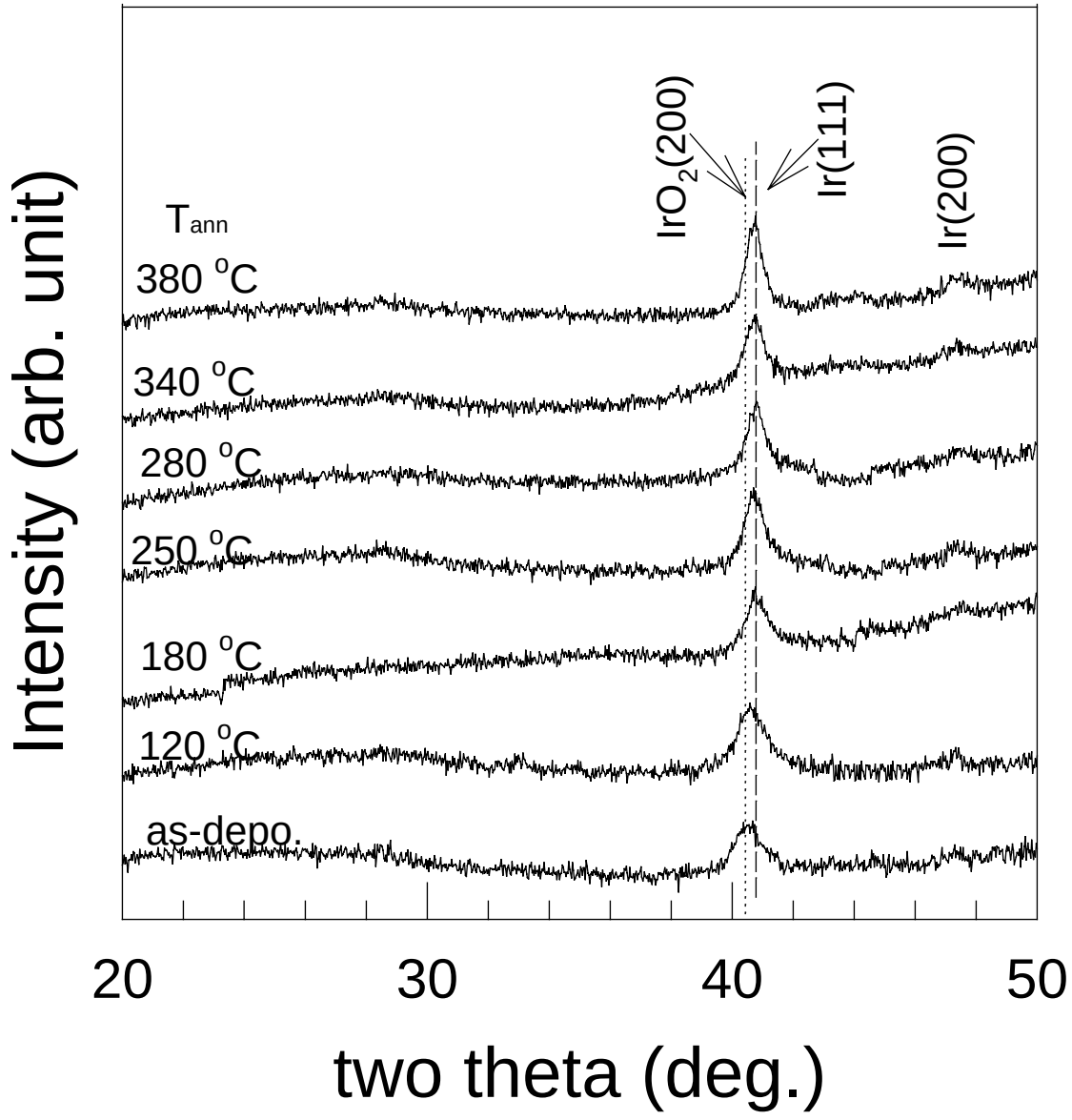

Fig. 3.7. XRD patterns of IrO_2/Ir/poly-Si annealed at different temperature (T_{ann}).

annealing of PZT layers was carried out at fixed T_{post} of 600 ^{o}C for all specimens (Fig. 3.6(c)). Figure 3.7 shows the XRD patterns of annealed IrO_2/Ir electrodes as a function of annealing temperature (T_{ann}). As the T_{ann} was increased, broad XRD peaks at around $2\theta=40.5^{o}$ shifted continuously towards higher angles of 2θ. It could be easily seen that these peaks have a shape formed by the superposition of two peaks, IrO_2(200) and Ir(111). Hence, the shift of this peak could be interpreted as enhanced crystallization of Ir and diminished growth of IrO_2 with the increase in T_{ann}.

Figure 3.8 shows the ratio of Ir/O on the surface of annealed IrO_2 (hereafter we refer 'annealed IrO_2' to 'IrO_x') as a function of T_{ann}. The values of x in IrO_x ranged from 0.65 to 0.45, which shows the appreciable reduction of oxygen concentration in as-deposited IrO_2 layer. As the T_{ann} increased from room temperature to 300 ^{o}C, oxygen content on the surface IrO_x layer was found to decrease significantly, owing to the escape of oxygen from the surface during the annealing process. However, in the annealing temperature regime of 300 ^{o}C to 400 ^{o}C, oxygen content on the surface was found to increase. This might be due to densification of IrO_x layer at these processing temperatures.

Figure 3.9(a) shows the typical AFM images ($2\times2\mu m^2$) of the surface morphology of IrO_x/Ir. From these AFM images, the surface area ratio of IrO_x/Ir electrodes, which is proportional to the surface roughness, was plotted as a function of annealing temperature in Fig. 3.9(b). The surface area ratio is calculated as a percentage of the three-dimensional surface area to the two-dimensional surface area produced by projecting surface onto a plane. It could be observed that IrO_x/Ir electrodes annealed at 280 ^{o}C possess the highest surface area ratio indicating a high surface area of these electrodes.

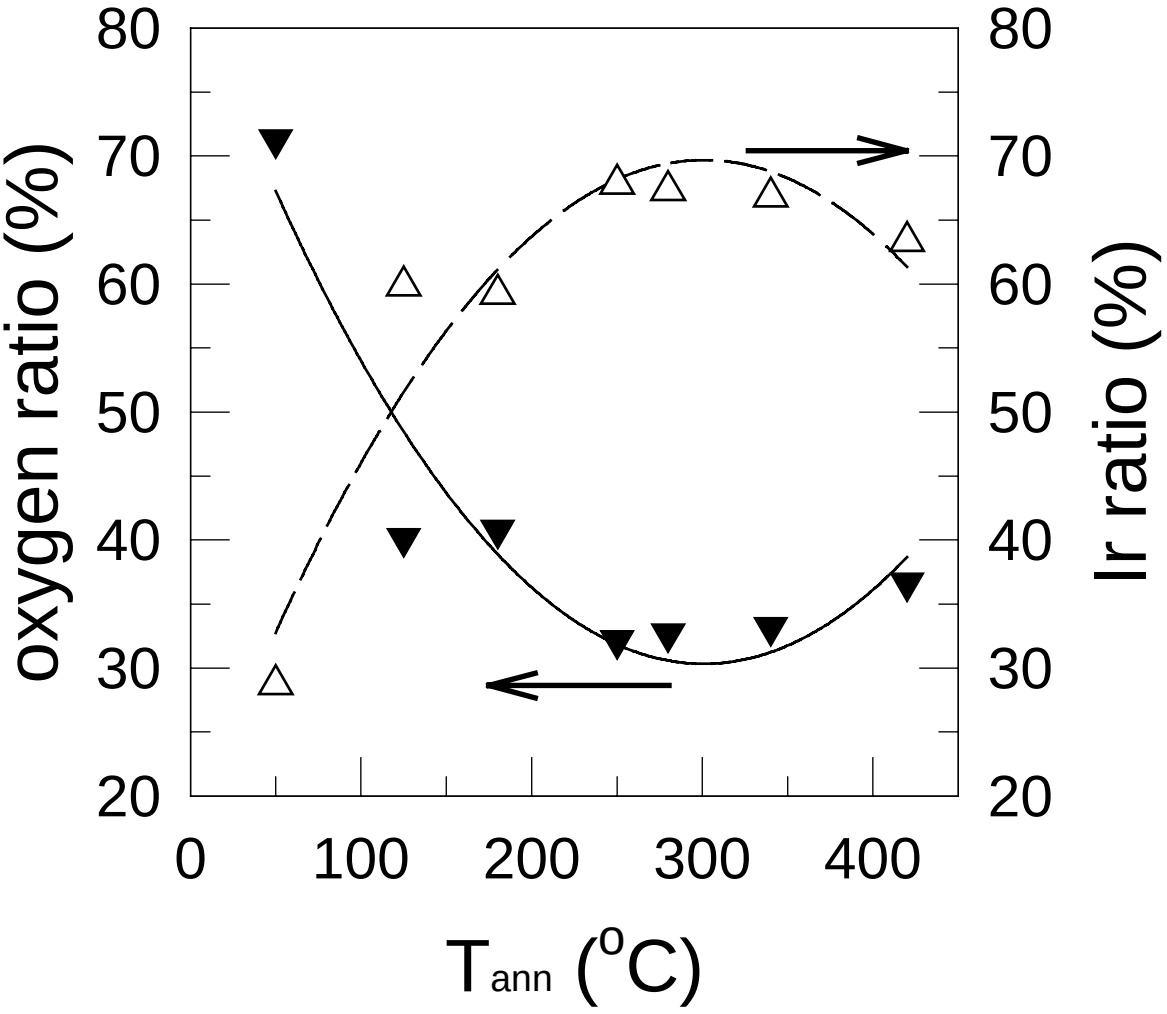

Fig. 3.8. Surface compositional ratio of Ir/O of IrO_x/Ir/poly-Si annealed at different T_{ann}.

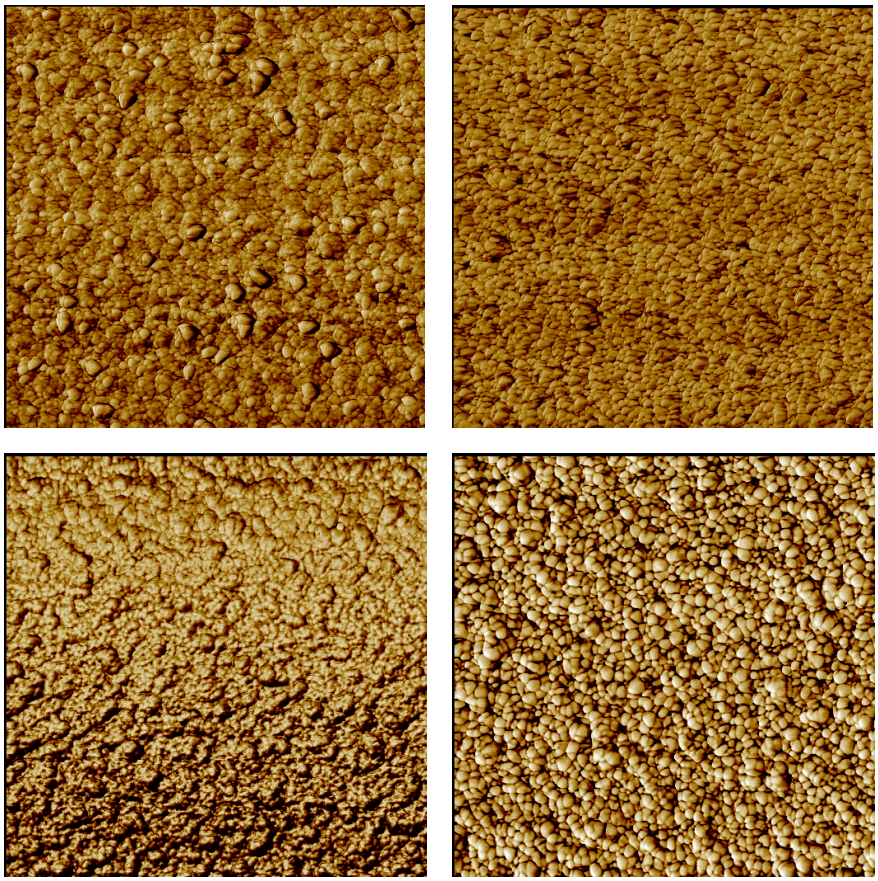

Fig. 3.9. (a) Typical AFM images of the surface morphologies of IrO_x/Ir with T_{ann}= (a1) 180^{o}C, (a2) 280^{o}C (a3) 340 ^{0}C and (a4) 380 ^{o}C

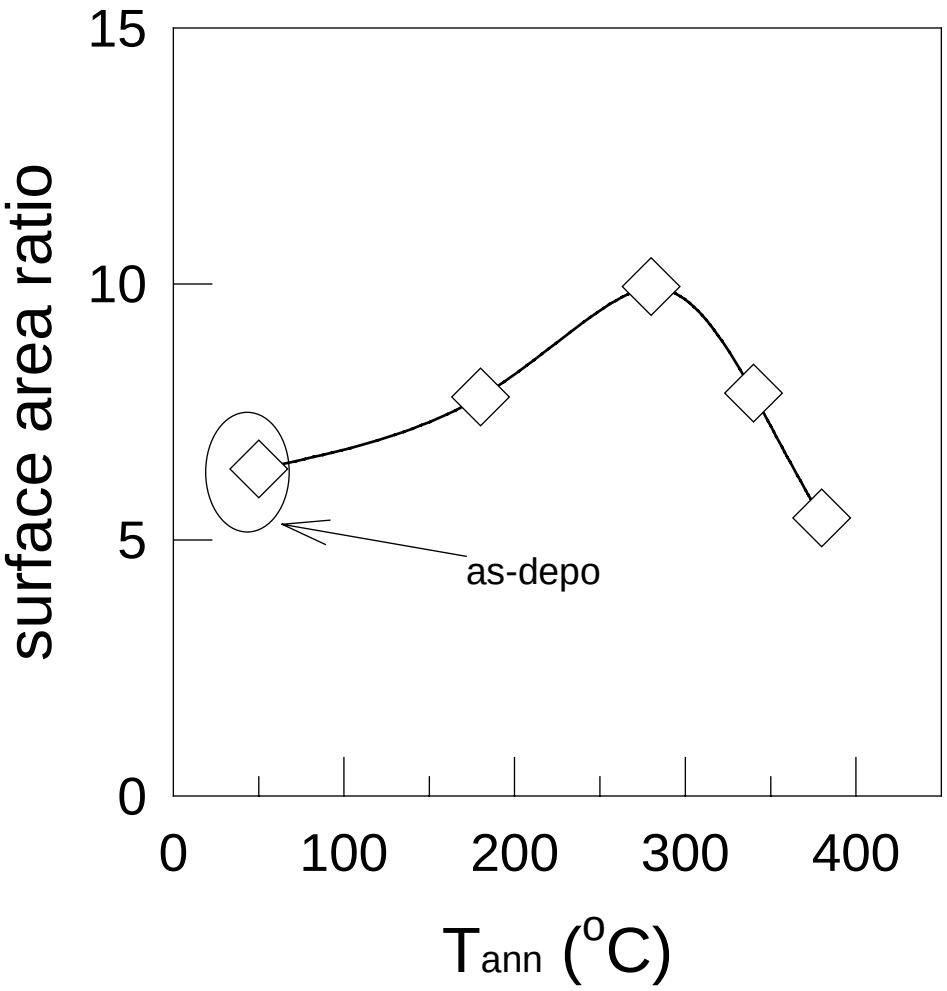

Fig. 3.9 (b) Plot of surface area ratio as a function of T_{ann}.

Hence, IrO_x/Ir electrodes annealed at 280 ^oC should possess a higher number of nucleation sites for the nucleation of perovskite phase of PZT thin films and hence, minimal amount of secondary phase should be seen in the PZT thin films deposited onto these IrO_x/Ir electrodes.

Fig 3.10 shows the XRD patterns of PZT thin films deposited on to these IrO_x/Ir bottom electrodes. It could be easily observed that the perovskite single phase without any pyrochlore phase was obtained in the PZT films deposited on IrO_x/Ir bottom electrodes annealed above 250 ^oC. As T_{ann} was increased from room temperature to 380 ^oC, maximum peak intensity of PZT(001) and PZT(002) had increased, while that of PZT(011) and PZT(111) were nearly constant. Although the XRD patterns as a function of T_{ann} could not be completely elucidated, it could be observed that PZT film deposited on annealed IrO_2/Ir electrodes have an increased tendency to orient along c-axis as T_{ann} was increased. In Fig. 3.10, it could also be seen that the integrated intensity of amorphous halos at around 2θ of 29^o decreased with the increase of T_{ann}, which nearly disappeared at T_{ann} = 280 ^oC. This result indicated that the intermediate layer formed by the reaction of PbO with IrO_2 as well as the second phase was successively diminished by means of the vacuum annealing of IrO_2/Ir bottom electrode before the deposition of PZT on it. This result could also be confirmed by the measurement of surface morphology of PZT films by AFM.

Figure 3.11 shows the typical AFM images of the surface morphology for PZT films deposited on annealed IrO_x/Ir processed at different T_{ann} of (a) 180 ^oC, (b) 280 ^oC and (c) 380 ^oC. While the AFM image for PZT film deposited on as-deposited IrO_2/Ir

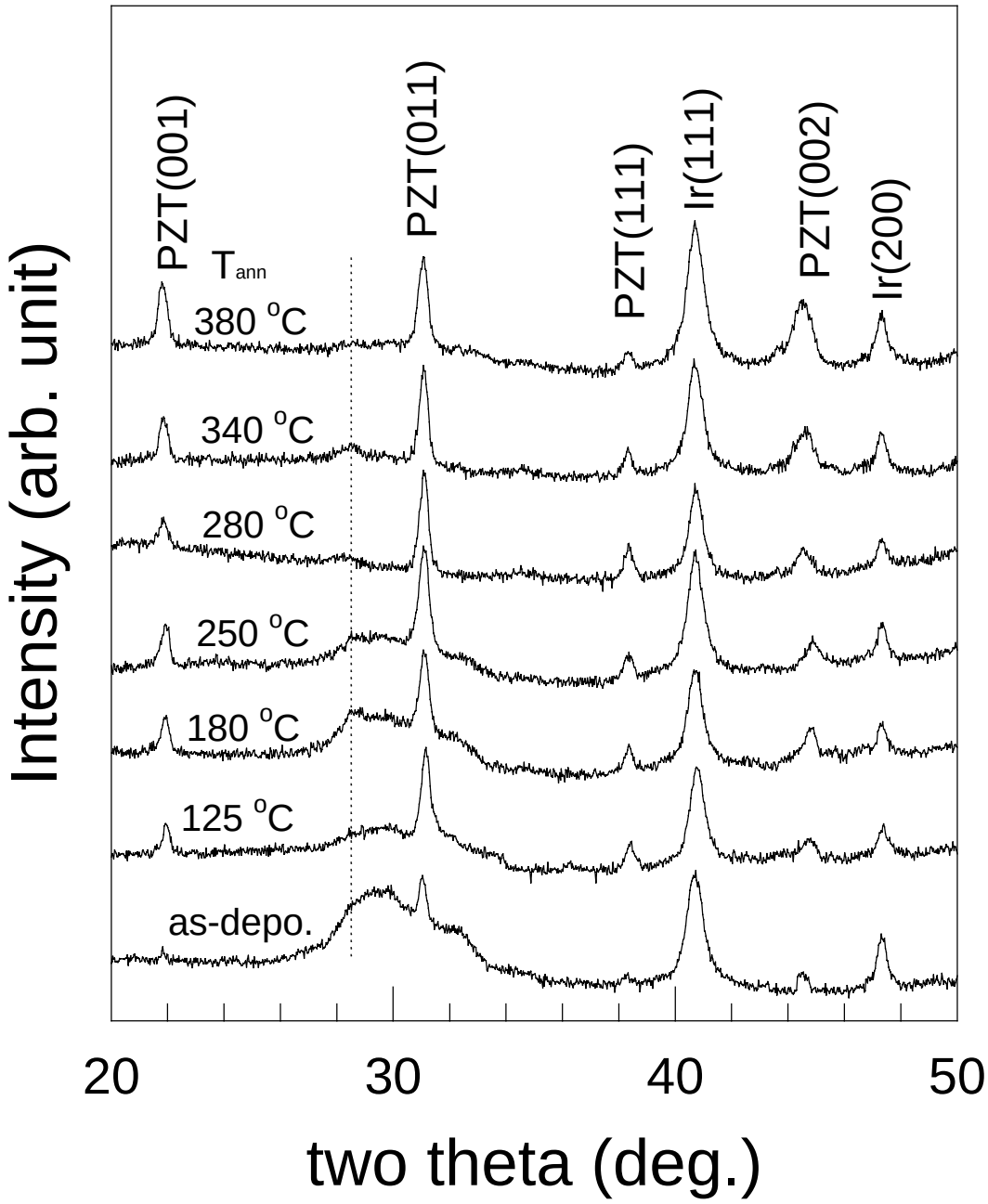

Fig. 3.10. XRD patterns of PZT thin films deposited on annealed IrO_2/Ir/poly-Si with different annealing temperatures.

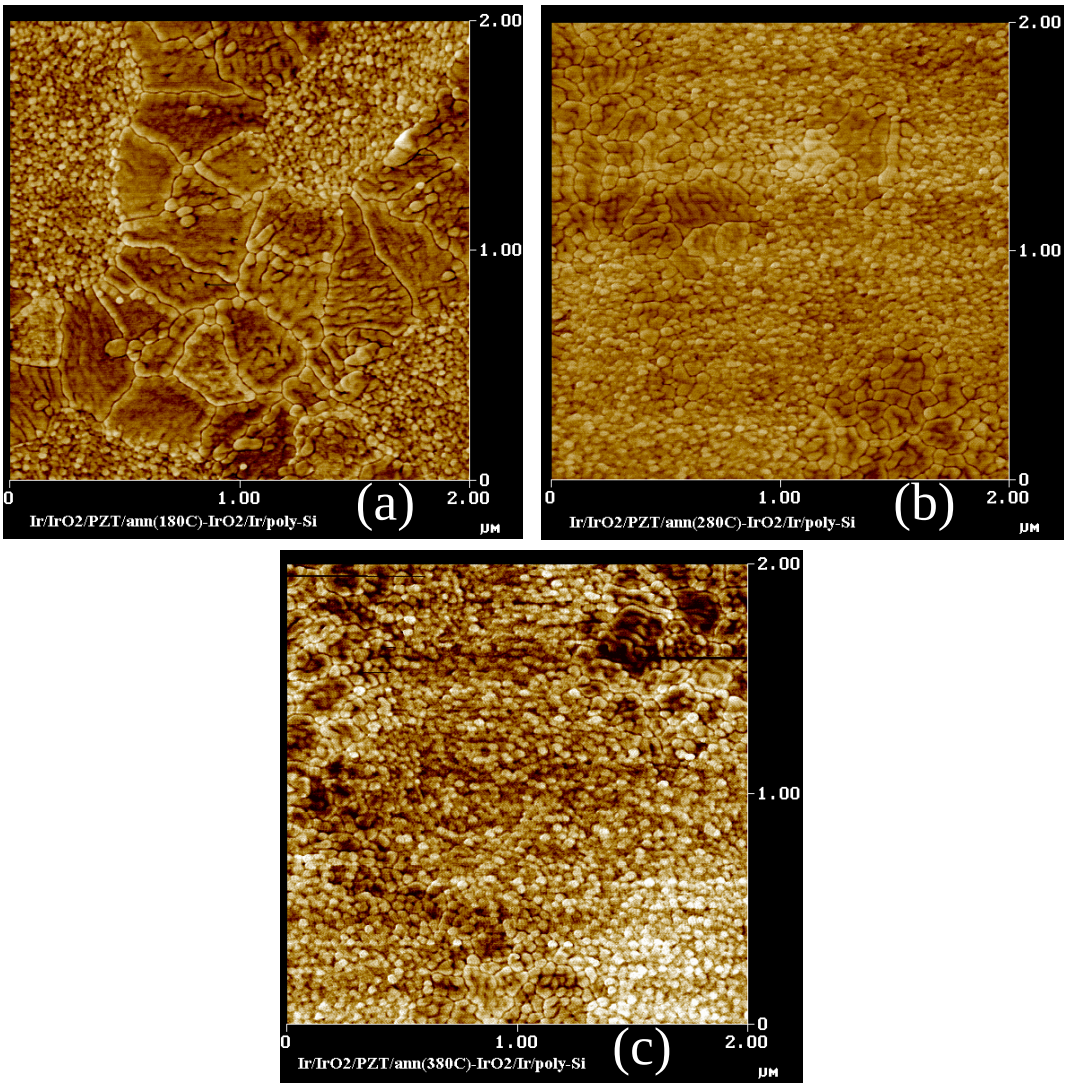

Fig. 3.11. Typical AFM images of the surface morphologies of PZT thin films deposited on annealed IrO_2/Ir/poly-Si with (a) T_{ann}=180^{o}C, (a) T_{ann}=280^{o}C and (c) T_{ann}=380 ^{o}C.

showed a second phase with a diameter greater than 5□□m (Fig. 3.2(a)), distribution and size of this second phase decreased as T_{ann} was increased and for T_{ann} greater than 280 ^{o}C, the second phase nearly disappeared. These results are remarkably compatible with those of XRD patterns of PZT films, as shown in Fig. 3.10. Hence, the results shown in Fig. 3.11 as well as in Fig. 3.10 indicate that by means of the vacuum annealing of IrO_2/Ir electrode before the depositing PZT layer significantly minimized the Pb-Ir-O reaction layer and also enhanced the perovskite phase in PZT films.

In order to investigate the effect of such microstructural changes in PZT layer deposited on to annealed IrO_2/Ir electrode on the electrical properties of PZT capacitors, P-E hysteresis loop, polarization fatigue and leakage current-voltage characteristics were measured. Figure 3.12 shows the typical P-E hysteresis loops of PZT capacitors with the bottom electrode processed at different T_{ann}. A well-defined P-E hysteresis loops were obtained for all the specimens. The same P-E loops were also obtained even if one electrical contact was replaced from the surface of poly-Si to the bottom-Ir electrode, which confirmed that annealed IrO_x/Ir bottom electrode behaved as a good electrode-barrier. Variation of P_r and E_c with T_{ann} is shown in Fig. 3.13. The value of P_r increased with the increase in T_{ann}, The value of P_r increased with the increase in T_{ann}, or T_{ann} below 180 ^{o}C, and decreased with the increase in T_{ann}, for T_{ann} above 180 ^{o}C. The maximum P_r value was about 20 $\mu C/cm^2$ for the PZT capacitor with annealed IrO_2/Ir bottom electrode, where T_{ann}=180 ^{o}C. However, E_c increased slightly with the increase in T_{ann}. Although both P_r and E_c of PZT capacitors are known to be related to the crystalline orientation and grain size of PZT, hysteresis behaviors with T_{ann} shown in Fig. 3.13 could not be easily

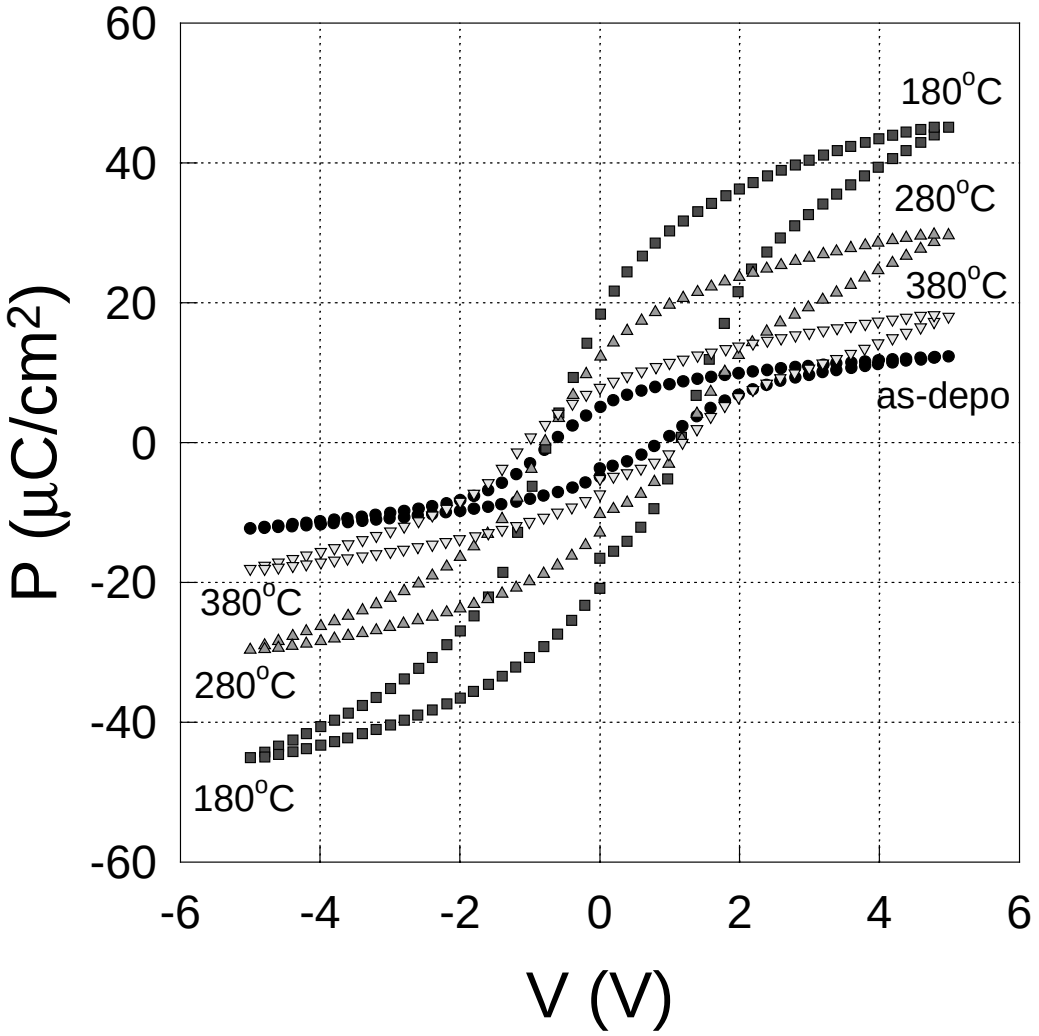

Fig. 3.12. Typical P-E hysteresis loops of Ir/IrO_2/PZT/annealed $IrO_2(T_{ann})$/Ir/poly-Si.

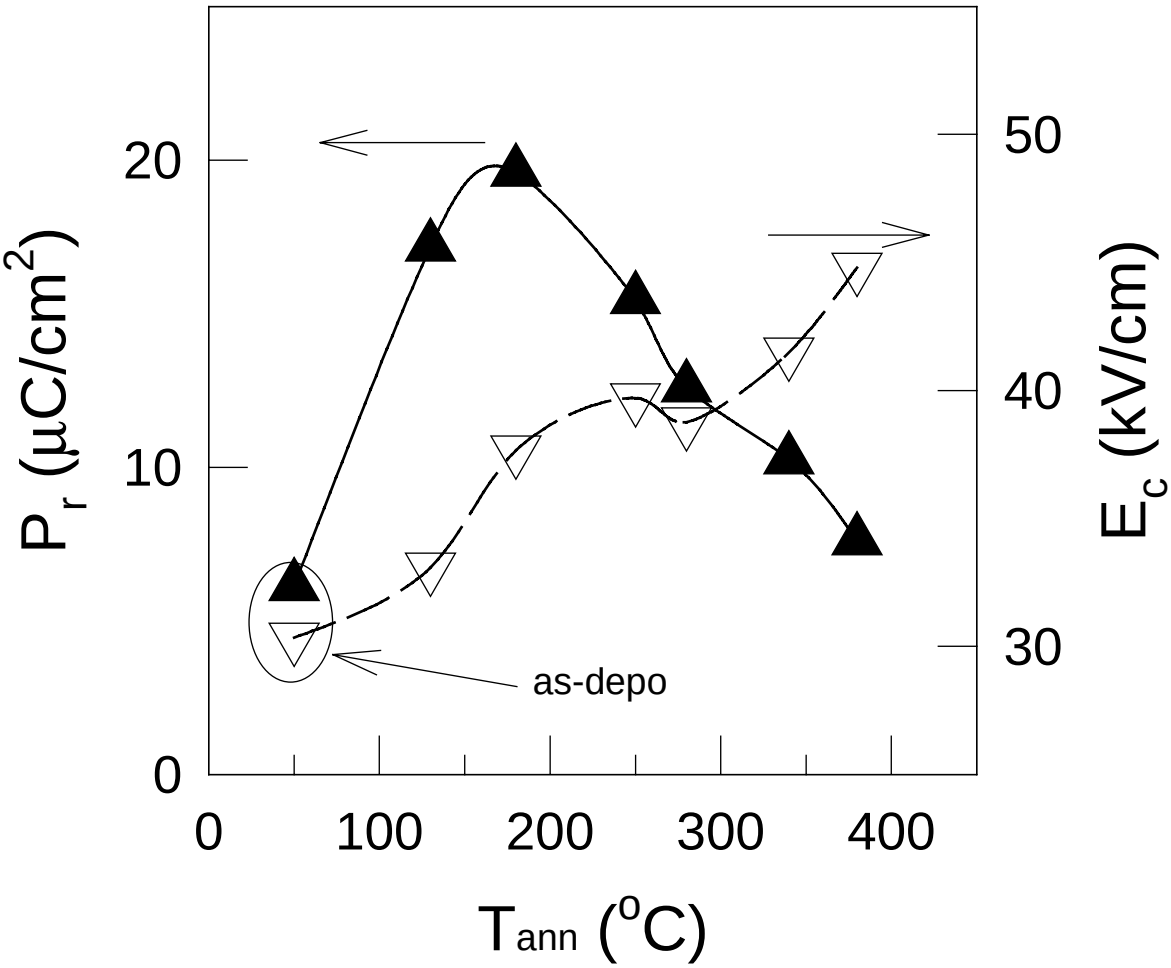

Fig. 3.13. Plot of P_r and E_c as a function of T_{ann}.

interpreted, since it is difficult to elucidate the relation of ferroelectric properties with the crystallinity of randomly oriented polycrystalline PZT films. Since, The focus of the present study is to minimize the fatigue of PZT based capacitors, more emphasis was put on fatigue and leakagae current behaviors of PZT capacitors with IrO_x/Ir electrodes processed at various temperatures.

Figure 3.14 shows the typical polarization-fatigue behaviors of PZT capacitors with annealed IrO_x/Ir bottom electrode processed at different T_{ann}. The polarization loss after 10^{11} switching repetitions was plotted as a function of T_{ann} in the inset of Fig. 3.14. It could be observed that fatigue behaviors of all PZT capacitors were improved as compared to those of PZT capacitors with as-deposited IrO_2/Ir electrode. Such a behavior could be attributed to the proper development of perovskite phase with minimal amounts of pyrochlore and secondary phases in these PZT films (Fig 2.10). Moreover, the plot of polarization loss *vs*. T_{ann} showed a minimum of 12% at T_{ann} = 280 ^oC, which could be explained based on the absence of any pyrochlore phase or secondary phases in the PZT films deposited on IrO_x/Ir electrode annealed at 280 ^oC (Fig. 3.10). Additionally, we found that the optimum T_{ann} could vary sensitively with the as-deposited IrO_2 thickness. For example, PZT capacitor with bottom electrode of IrO_2(40nm)/Ir with T_{ann}=300 ^oC showed a high polarization loss of 50%.

Figure 3.15 shows the typical I-V characteristics of PZT capacitors with annealed IrO_x/Ir bottom electrode-barrier as well as with as-deposited IrO_2/Ir. It could be easily seen that the leakage current density of PZT capacitor decreased with the increase of T_{ann}. In addition, the intermediate region was shifted towards higher fields as T_{ann} increased and then disappeared at T_{ann} larger than 280 ^oC. I-V behaviors of PZT capacitors with

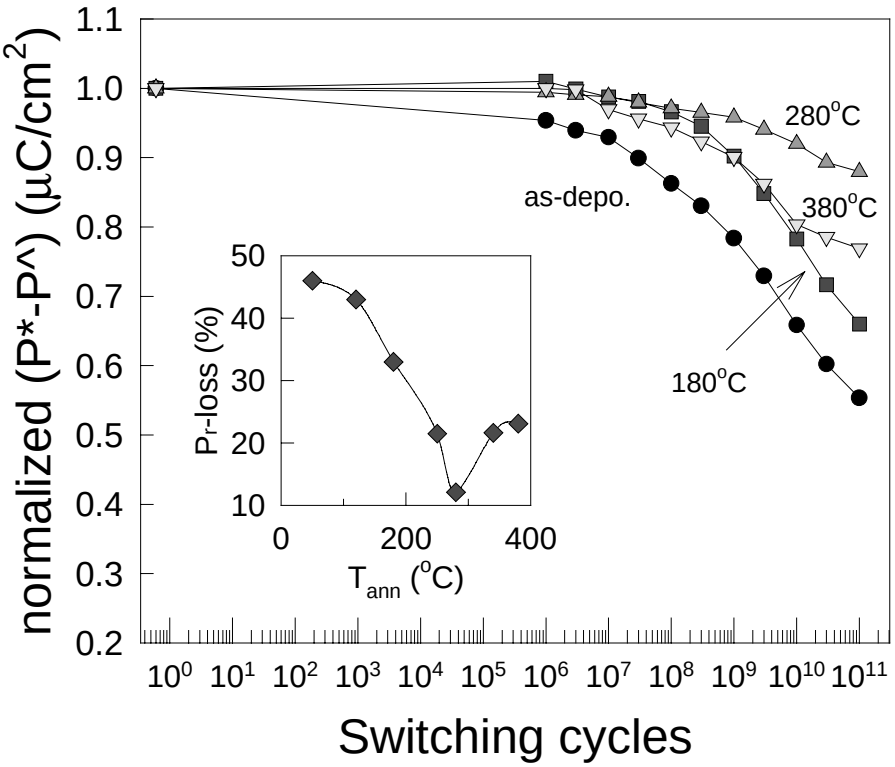

Fig. 3.14. Typical polarization-fatigue behaviors of $Ir/IrO_2/PZT/$annealed $IrO_2/Ir/$poly-Si capacitors. The inset shows the polarization loss after 10^{11} switching cycles plotted as a function of T_{ann}.

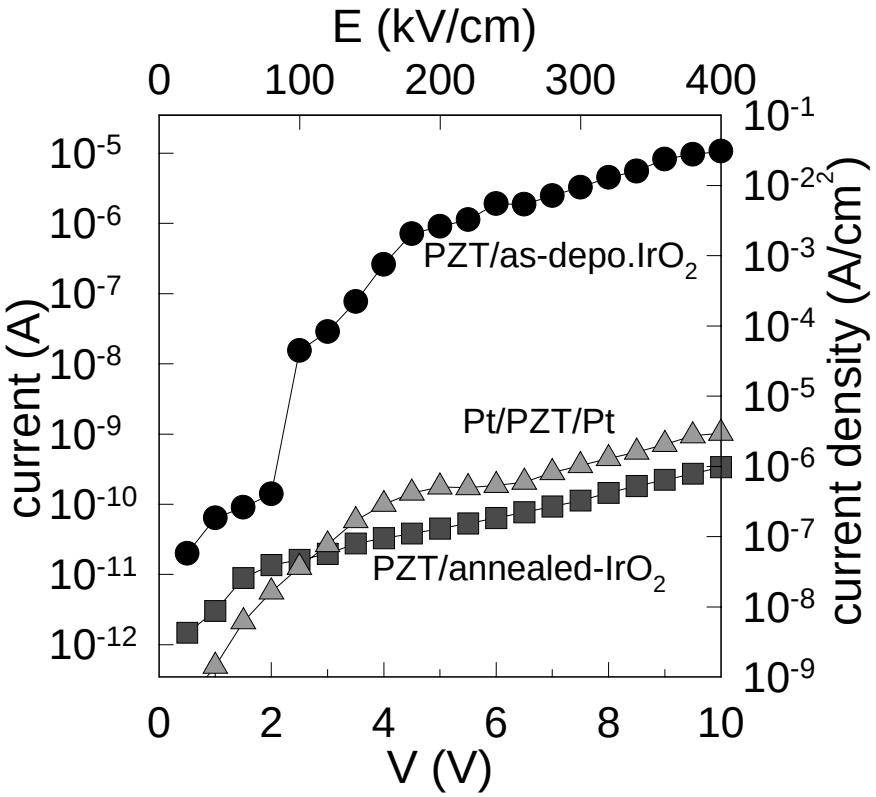

Fig. 3.15. Typical leakage current-voltage characteristics of Ir/IrO_2/PZT/annealed IrO_2/Ir/poly-Si capacitors with different T_{ann}.

T_{ann} higher than 280 ^{o}C were shown to be intrinsic, which might be dominated by Schottky emission[15,16]. Leakage current densities of PZT capacitors with IrO_x/Ir bottom electrode annealed at T_{ann} greater than 280 ^{o}C were about $1x10^{-7}$ A/cm^2 at an applied field of 200 kV/cm, which is comparable to the leakage current

density of Pt/PZT/Pt capacitor, as shown in Fig. 3.4. Such improvements in the behaviors of both leakage current and polarization fatigue are due to the reduction of the secondary phases as well as the intermediate layer which arises from the reaction between PbO in PZT and IrO_x near the interface between PZT/bottom-electrode.

Figures 3.16(a) and (b) show the AES depth profiles of PZT/annealed IrO_2/Ir(T_{ann}=280^{o}C)/poly-Si and PZT/Pt/Ti/SiO_2/Si, respectively. The measurements of AES depth profile were performed at a sputtering rate of about 2.5 nm/min. During AES depth profile measurement, more emphasis was put on the oxygen profiles in PZT bulk and near the interface between PZT and Pt than on the profiles of the other elements, such as Pb and Zr, since Pb and Zr interfered with Ir in AES analysis. Oxygen depth profiles were found to be quite different in PZT thin films deposited on different bottom electrodes. PZT thin films deposited on annealed IrO_2/Ir bottom electrode were found to possess nearly constant oxygen concentration with depth (Fig. 3.16(a)), while PZT thin film deposited on a Pt/Ti/SiO_2/Si substrate possessed an apparently decreasing oxygen concentration as the interface of PZT and Pt was approached (Fig. 3.16(b)). Scott *et al.*[17] noticed a loss of polarization as well as a decrease in the oxygen concentration near the electrodes after fatigue cycling, which indicated an increased accumulation of oxygen vacancies. Additionally, a quantitative fatigue model proposed by Desu[18] predicted that fatigue could be minimized by preventing space charge formation arising out of oxygen

vacancies at the interface. This model explained our results that PZT/Pt/Ti/SiO_2/Si, which contained higher oxygen vacancies at the PZT/Pt interface, exhibited a lower fatigue resistance as compared to that of PZT/annealed IrO_x/Ir/poly-Si which contained lower oxygen vacancies at the interface.

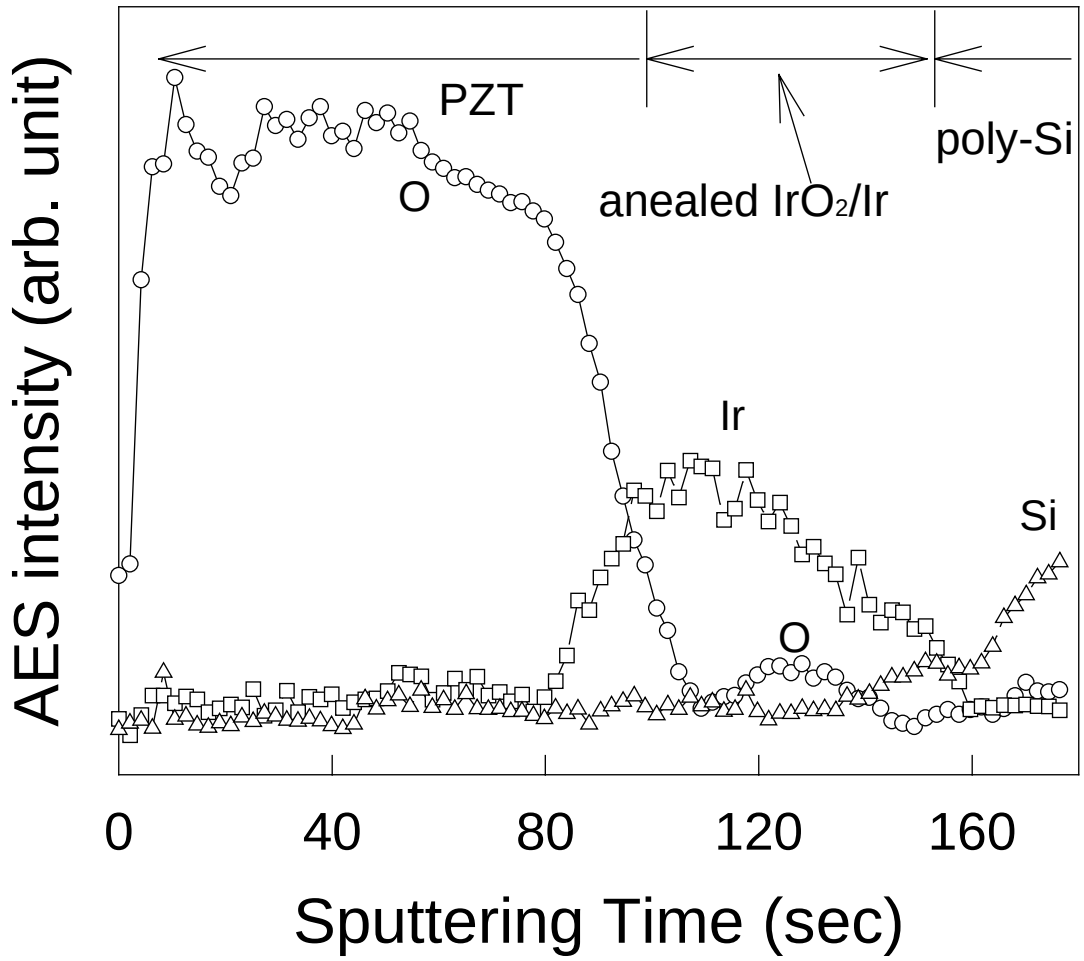

Fig. 3.16(a). AES depth profiles of oxygen in PZT thin film deposited on annealed-IrO_2/Ir/poly-Si with T_{ann}=280 ^oC

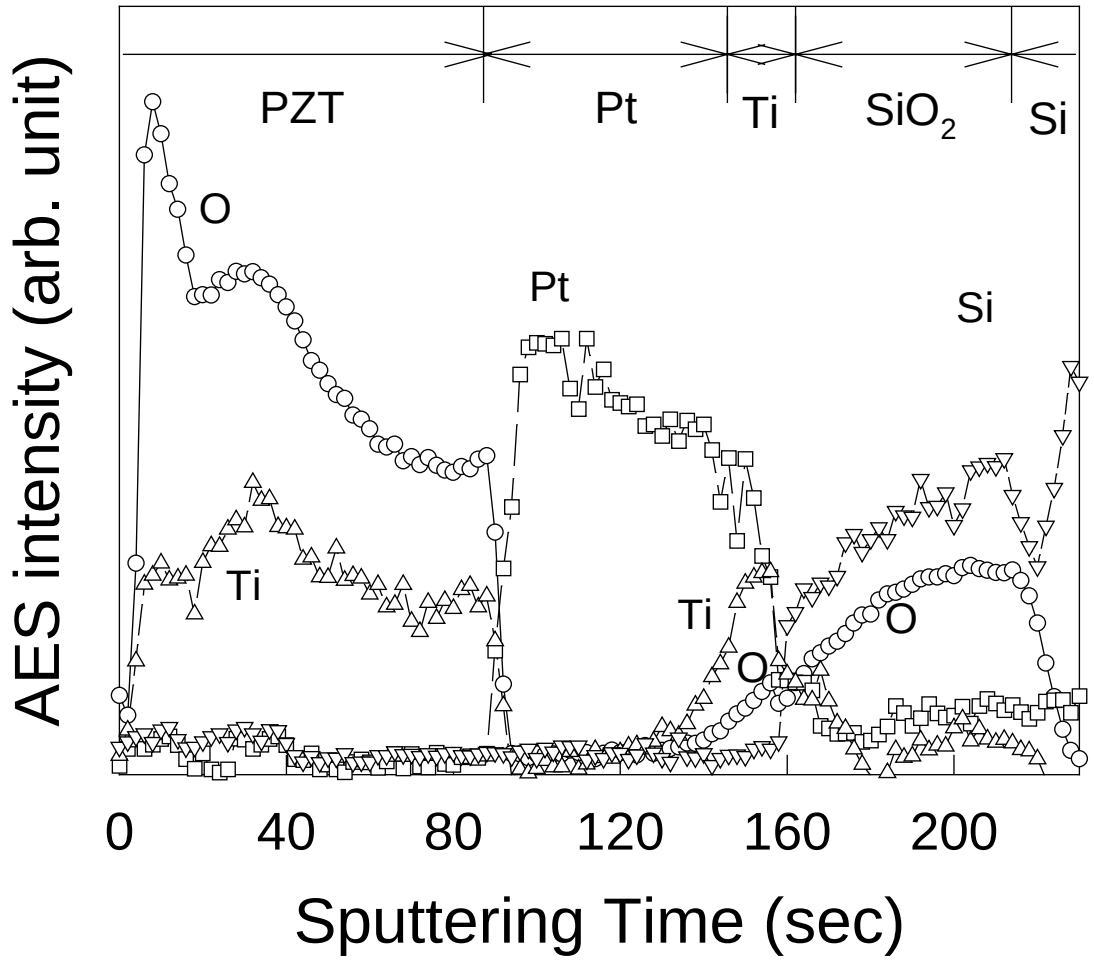

3.16(b). AES depth profiles of oxygen in PZT thin film deposited on Pt/Ti/SiO_2/Si, where the sputtering rate was about 2.5 nm/min.

3. 4. Conclusion

A simple electrode-barrier using Ir was investigated and developed for the preparation of PZT-based nonvolatile memories. PZT thin films were deposited on to sputter deposited IrO_2/Ir electrodes. While the PZT thin films annealed at a lower temperature of 650 ^oC possessed pyrochlore phase, films annealed at a higher temperature of 700 ^oC possessed intermediate reaction layers of Pb-Ir-O at the interface, and also secondary phases, which formed due to the imbalance in the stoichiometry of PZT thin films at these high processing temperatures. Consequently, PZT capacitors prepared by using as-deposited IrO_2/Ir electrodes exhibited poor fatigue and leakage current behaviors. By means of annealing of IrO_2/Ir bottom electrodes, the microstructural development of PZT thin films was carefully controlled to obtain perovskite rich films. Additionally, the intermediate reaction layers and the secondary phases were eliminated resulting in high quality PZT thin film capacitor, which has a structure of Ir/IrO_2/PZT/annealed IrO_x/Ir/poly-Si. Annealed IrO_2/Ir layer itself behaved as an excellent high temperature electrode-barrier, and PZT capacitor with such electrode-barrier structure showed a significant increase of fatigue resistance as well as leakage resistivity. PZT capacitors deposited on annealed IrO_2(T_{ann}=280^oC)/Ir electrodes were found to possess a remanent polarization and a polarization loss of 13 □C/cm^2 and 12 % after 10^{11} switching repetitions, respectively, and leakage current density of 1x10^{-7} A/cm^2 at an applied field of 200 kV/cm. The electrode-barrier properties of this simple electrode structure should make it possible to integrate ferroelectric PZT capacitors with high density nonvolatile memory cell structures. In this paper, we have shown that use of

oxide electrodes alone does not necessarily improve the fatigue resistance of PZT capacitors. Development of perovskite rich microstructure of PZT films plays an equally important role in governing the fatigue and leakage behaviors of PZT capacitors.

References

1. R. Rameshi, W. K. Chan, B. Wiikens, H. Gilchrist, T. Sands, J. M. Tarascon, V. G. Keramdas, D. K. Fork, J. Lee, and A. Safari, Appl. Phys. Lett. **61**, 1537(1992).

2. S. Yokoyama, Y. Ito, K. Ishhara, K. Hamada, S. Ohnishi, J. Kudo, and K. Sakiyama, Jpn. J. Appl. Phys. Part 1 **24**, 767(1995).

3. R. Ramesh, J. Lee, T. Sands, and V. G. Keramdas, Appl. Phys. Lett. **64**, 2511(1994).

4. I. K. Yoo, S. B. Desu and J. Xing, *Ferroelectric Thin Films III*, (Mater. Res. Soc. Symp. Proc. **310**, Pittsburg, 1993) p. 165.

5. K. Aoki, Y. Fukuda, K. Numata and A. Nishimura, Jpn. J. Appl. Phys. **34**, 5250(1995).

6. H. N. Al-Shareef, O. Auciello and A. I. Kingon, J. Appl. Phys. **77**, 2146(1995).

7. T. Nakamura, Y. Nakao, A. Kamisawa and H. Takasu, Appl. Phys. Lett. **65**, 1522(1994).

8. H. D. Bhatt, S. B. Desu, D. P. Vijay, Y. S. Hwang, X. Zhang, M. Nakata, and A. Grill, Appl. Phys. Lett. **71**, 719(1997).

9. K. B. Lee, Y. Song, S. Tirumala and S. B. Desu, Appl Phys. Lett. (1998) submitted.

10. Y. Jeon, J. Seon, J. Joo, K. Oh, J. Roh, and D. Kim, Appl. Phys. Lett. **71**, 467(1997).

11. Y. Song, Y. Zhu, and S. B. Desu, Appl. Phys. Lett. **72**, 2686(1998).

12. M. Shimizu, H. Fujisawa, S. Hyodo, S. Nakashima, H. Niu, H. Okino and T. Shiosaki, *Ferroelectric Thin Films IV*, (Mater. Res. Soc. Symp. Proc. **493**, Boston, 1997) p. 159.

13. W. L. Warrant, D. Dimos and R. M. Waser, MRS bulletin **21**, 40(1996).

14. I. L. Chung, S. B. Desu, and D. P. Vijay, Mater. Res. Soc. Symp. Proc. **361**, 241(1995).

15. G. W. Dietz, M. Schumacher, R. Waser, S. K. Streiffer, C. Basceri and A. I. Kingon, J. Appl. Phys. **82**, 2359(1997).

16. T. Mihara and H. Watanabe, Jpn. J. Appl. Phys. **34**, 5664(1995).

17. J. F. Scott, C. A. Araujo, B. M. Melnick, L. D. McMillan, and R. Zuleeg, J. Appl. Phys. **70**, 382(1991).

18. S. B. Desu, Phys. Stat. Sol. (a) **151**, 467(1995).